Characterizing Tundra snow sub-pixel variability to improve brightness temperature estimation in satellite SWE retrievals

Julien Meloche[1,2], Alexandre Langlois[1,2], Nick Rutter[3], Alain Royer [1,2], Josh King[4], Branden Walker[5], Philip Marsh[5], Evan J. Wilcox[5]

[1]Centre d'Applications et de Recherche en Télédétection, Université de Sherbrooke, Sherbrooke, J1K 2R1, Canada
[2]Centre d'études Nordiques, Université Laval, Québec, G1V 0A6, Canada
[3]Department of Geography and Environmental Sciences, Northumbria University, Newcastle upon Tyne, NE1 8ST, UK
[4]Environment and Climate Change Canada, Climate Research Division, Toronto, M3H 5T4, Canada
[5] Cold Regions Research Centre, Wilfrid Laurier University, Waterloo, N2L 3C5, Canada

Corresponding author: Julien Meloche (julien.meloche@usherbrooke.ca)

Abstract.

Topography and vegetation play a major role in sub-pixel variability of Arctic snowpack properties, but are not considered in current passive microwave (PMW) satellite SWE retrievals. Simulation of sub-pixel variability of snow properties is also problematic when downscaling snow and climate models. In this study, we simplified observed variability of snowpack properties (depth, density, microstructure) in a two-layer model with mean values and distributions of two multi-year tundra dataset so they could be incorporated in SWE retrieval schemes. Spatial variation of snow depth was parametrized by a log-normal distribution with mean (μ_{sd}) values and coefficients of variation (CV_{sd}). Snow depth variability (CV_{sd}) was found to increase as a function of the area measured by a Remotely Piloted Aircraft System (RPAS). Distributions of snow specific surface area (SSA) and density were found for the wind slab (WS) and depth hoar (DH) layers. The mean depth hoar fraction (DHF) was found to be higher in Trail Valley Creek (TVC) than in Cambridge Bay (CB) where TVC is at a lower latitude with a sub-arctic shrub tundra compared to CB which is a graminoid tundra. DHF were fitted with a gaussian process and predicted from snow depth. Simulations of brightness temperatures using the Snow Microwave Radiative Transfer (SMRT) model incorporating snow depth and DHF variation were evaluated with measurements from the Special Sensor Microwave/Imager and Sounder (SSMIS) sensor. Variation in snow depth (CV_{sd}) is proposed as an effective parameter to account for sub-pixel variability in PMW emission, improving simulation by 8K. SMRT simulations using a CV_{sd} of 0.9 best matched CV_{sd} observations from spatial datasets for areas > 3 km^2, which is comparable to the 3.125 km pixel size of the Equal-Area Scalable Earth (EASE) grid 2.0 enhanced resolution at 37 GHz.

Keywords: sub-pixel variability, microwave, snow water equivalent, tundra snow

1 Introduction

Snow cover is known to be highly variable at the local scale (10 – 1000 m) due to wind redistribution, sublimation (Liston and Sturm, 1998; Winstral et al., 2013) and vegetation trapping (Sturm et al., 2001). Physical properties of snow such as measurement of stratigraphy (Fierz et al., 2009) can be aggregated into layers, but their spatial distribution is highly variable given their dependence on total depth and surface roughness (Liljedahl et al., 2016; Rutter et al., 2014). Such variability leads to uncertainties in the retrievals of snow state variables such as snow water equivalent (SWE) using microwave remote sensing from local scales (King et al., 2018; Rutter et al., 2019) to global scales (Pulliainen et al., 2020). Improving our empirical understanding of the processes governing this variability would improve space-borne snow monitoring, especially in Arctic regions where ground measurements and weather station networks are sparse.

Measurement of SWE using passive microwave satellite data (Larue et al., 2018; Pulliainen, 2006) is possible using a radiative transfer model to simulate snow emission at various frequencies, from which an inversion of the model can produce global estimates of snow depth (Takala et al., 2011). More specifically, passive microwave brightness temperatures (T_B) are governed by radiometric properties of the layered snowpack. As such, each layer has its own absorption and scattering properties; the amount of scattering is proportional to snow total mass where the scattering and emission is frequency-dependent (Kelly et al., 2003). Scattering at higher frequencies such as 37GHz, will lead to lower T_B so differences between T_B at two frequencies (37-19 GHz) is related to snow mass (Chang et al., 1982). Arctic snowpack mainly consists of two distinct layers (wind slab and depth hoar), where each layer has unique scattering properties (Derksen et al., 2010). Complexity of the layered properties (density, temperature and microstructure) strongly influence radiative transfer modelling (King et al., 2015; Rutter et al., 2014). Furthermore, recent developments in radiative transfer modelling (SMRT: Picard et al., 2018, DMRT: Tsang et al., 2000 and MEMLS: Wiesmann and Mätzler, 1999), microstructure representation (Royer et al., 2017), and in situ measurement of snowpack properties (Gallet et al., 2009; Montpetit et al., 2012; Proksch et al., 2015) have provided significant agreement between models and in situ measurements. However, spatial distribution and heterogeneity of total snow depth and stratigraphy remains challenging to implement and is not considered for large scale monitoring of SWE in tundra environments. Rutter et al. (2019) and Saberi et al. (2020), using three- and two-layer models respectively, demonstrated a relationship between the ratio of depth hoar and wind slab with respect to total depth, enabling the usage of proportion of these two layers with total snow depth. Working with a simplified layer representation of a snowpack with well-defined physical properties may adequately characterize snowpack for large scale SWE retrievals.

Two dominant processes governing snow depth variability in the Arctic are 1) wind redistribution with topography (Sturm and Wagner, 2010; Winstral et al., 2002) and 2) vegetation trapping (Domine et al., 2018; Sturm et al., 2001). Liston (2004) described snow depth heterogeneity using a log-normal distribution with a coefficient of variation of snow depth (CV_{sd}), the ratio between standard deviation (σ_{sd}) and the mean of snow depth (μ_{sd}), indicating the extent and spread of a distribution (i.e. high variability over thin snow will lead to high values of CV_{sd}). Also, Liston (2004) proposed 9 categories of CV_{sd} with

values ranging from 0.9 to 0.06 for mid-latitude treeless mountains to ephemeral snow, where arctic tundra type was 0.4. Snow depth variability is based on a parametrization of μ_{sd}, CV_{sd} on the log-normal distribution scale parameters (λ, ζ). Gisnas et al. (2016) adapted that approach using scale parameters (α, β) of the gamma distribution. In all cases, CV_{sd} is used to describe subgrid variability (Clark et al., 2011), but its value remains challenging to quantify given that regional trends are linked to topography, vegetation and climate (Winstral and Marks, 2014). In this context, CV_{sd} is used to quantify spatial heterogeneity of snow in climate modelling, but so far has not been used in microwave SWE retrievals.

In SWE retrievals, snow depth is assumed to be uniform and the mean depth is used to optimize brightness temperature and derive SWE from depth and assumed density (Kelly, 2009). There is potential for CV_{sd} to be used as an effective parameter to estimate sub-pixel variability in brightness temperature. Bayesian frameworks are used in inversion schemes for SWE retrievals (Durand and Liu, 2012; Pan et al., 2017; Saberi et al., 2020) using *a priori* information (density, microstructure and temperature) from regional snowpack characteristics and inversion of radiative transfer models (Saberi et al., 2020). An iterative approach based on Bayesian theory is used (Takala et al., 2011) to match observed brightness temperature with modelled brightness temperature by iterating *a priori* information of the snowpack in order to derive snow depth and SWE. Saberi et al. (2020) conducted a case study for snow depth retrievals using a two layer model from airborne microwave observations using a Bayesian framework (or Markov Chain Monte Carlo) over tundra snow. However, high uncertainty (21.8 cm) in retrieved snow depth (via T_B) resulted, which suggested the use of a term involving variation in snow depth and microstructure within the footprint instead of a uniform snow depth.

To address this research gap, we used a multi-year snow dataset from two Arctic locations to quantify sub-pixel variability of snow depth and microstructure and used CV_{sd} as an effective parameter that controls snow sub-pixel variability. Firstly, we evaluate tundra snow depth spatial variability using probability density functions (log-normal and gamma) and its parameters, μ_{sd} and CV_{sd}. Secondly, we present from in-situ observations distinct snow microstructure and density values of both tundra main layers (depth hoar and wind slab), mean ratios of layer thickness and the depth hoar fraction (DHF) relative to snow depth. Finally, we perform a Gaussian process fit to estimate DHF from snow depth and used probability density functions of snow depth to add variation of snow depth and microstructure within the footprint. Then we compare mean pixel snow properties simulations with simulations of sub-pixel variation in snow properties to evaluate biases between measured T_B from a satellite sensor at 19 and 37 GHz, and T_B simulated by inversion of a radiative transfer model.

2 Methods

2.1 Study site

Data were collected in two regions of the Canadian Arctic, with different topography and vegetation yielding different snow depth distributions. Trail Valley Creek (TVC) research watershed, Northwest Territories (68°44' N, 133°33' W), located at

the southern edge of arctic shrub-tundra, is dominated by herbaceous tundra and dwarf shrubs and characterized by gently rolling hills with steep slopes. Greiner Lake watershed, Cambridge Bay (CB), Nunavut (69°13' N, 104°53' W), located within arctic tundra, is characterized by dwarf shrub and calcareous tills on upland sites with gently rolling hills and small ponds and

95 lakes. TVC is considered to have more sub-arctic attributes with predominant vegetation than CB given its proximity to the Northern edge of the boreal forest. Topographic maps (Figure 1; ArcticDEM), show slightly higher variation in elevation at TVC with plateau and steep slopes compared to CB which is dominated by ponds and small variation in topography.
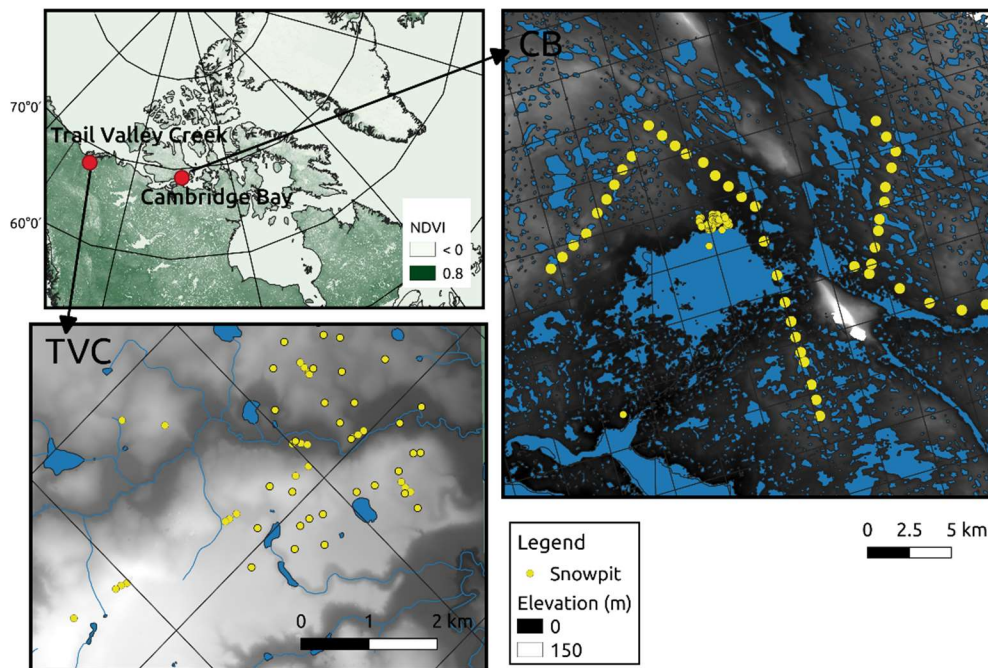
Figure 1: Locations of study areas in the Canadian Arctic, Cambridge Bay and Trail Valley Creek site. Grid shown is the
100 **enhanced 3.125 km EASE grid 2.0 used for satellite data. The ArcticDEM is a 2 m-resolution (Morin et al., 2016) derived from stereo high-resolution visible imagery for the entire Arctic domain, freely available.**

2.2 Data

Snow pits (315) at each site (TVC: 68, CB: 248) provided information on snow layering, vertical profiles of geophysical properties (includes temperature, grain type classification, hardness, density, microstructure, and depth). Measurements of

105 visual stratigraphy and grain type classification was conducted following Fierz et al. (2009). Density was measured using 100 cm^3 density cutters and digital scales. Snow specific surface area (SSA) was measured using an InfraRed Integrating Sphere (IRIS) (Montpetit et al., 2012b) in Cambridge Bay, and an A2 Photonic Sensors IceCube in TVC, both based on 1300 nm laser reflectometry (Gallet et al., 2009). Snow depth measurements, linear transects and circular transect around snow pits, used a

magnaprobe from SnowHydro LLC (Sturm and Holmgren, 2018), which is equipped with a standard GPS unit. Measured

110 snow depth distributions were used to identify subsequent pit locations (on site) from a predefined transect across CB watershed in order to ensure the snow pit locations were representative of wider spatial variability (Table 1). For TVC, pit locations were chosen based on previous snow depth distribution (2016), slope and elevation. Multiple snow depth maps at 1m resolution from Remotely Piloted Aircraft System (RPAS) surveys derived from photogrammetry conducted in March 2018 (Walker et al., 2020) were used to estimate snow depth distribution in TVC with total spatial coverage of 5.3 km^2. An

115 airborne Lidar dataset of TVC snow depths (93 km^2 at 10 m resolution) collected by an aircraft in April 2013 (Rutter et al., 2019) was also used. Monte Carlo simulations of both the μ_{sd} and CV_{sd} were performed on each snow depth map. Simulations randomly selected pixels as the center of a circular mask with a random radius. The mask was used to select all pixels within the circle so the statistical parameters (μ_{sd} and CV_{sd}) could be calculated. Also, a small RPAS map was available for CB with spatial coverage of 0.2 km^2 at 1 m resolution. Maps of normalized difference vegetation index (NDVI) were created from

120 Sentinel-2 (10 m resolution) images from late summer (2019-09-01 for TVC and 2019-09-08 for CB).

Table 1: Summary of number of snow depth measurements (Magnaprobe and RPAS) and snow pit sites per year. The availability of SSA and density measurements across sites and years are also noted (x). See Table 2 for full dates.

Site	Date	Depth Measurement	Snowpit	SSA	Density
TVC	March 15 -25, 2019	8541	32	x	x
	March 15 -23, 2018	7190	36	x	x
TVC18-RPAS	March 12- April 22, 2018	Pixels : 6 325 365 Resolution: 1 m			
TVC13-Lidar	April, 2013	Pixels : 969 168 Resolution: 10 m			
CB18-RPAS	April 15, 2018	Pixels : 72 902 Resolution: 1 m			
CB	April 15-29, 2019	982	64	x	x
	April 12-24, 2018	-	50	x	x
	May 1-8, 2017	4045	51		x
	April 2-10, 2016	3403	35		x
	April 9-16, 2015	12 282	48		x

125

2.3 Measured brightness temperatures and Snow Microwave Radiative Transfer (SMRT)

Microwave T_B were used to evaluate simulations from SMRT at 37 GHz and 19 GHz from the Special Sensor Microwave/Imager and Sounder (SSMIS) sensor, with the Equal-Area Scalable Earth (EASE) 2.0 grid resampled at 3.125 km (6.25 km for 19 GHz) resolution (Brodzik et al., 2018), for both TVC and CB regions. T_B were estimated by averaging all

130   pixels within snow pit area (CB: 24 pixels, TVC: 8 pixels for 37 GHz). Each pixel with at least one snow pit inside was used. Since all snow pits were aggregated to obtain mean value and distribution of snow properties for SMRT, averaged T_B covering the snow pits area was used.

The area was also filtered to remove any contribution from sea or deep lakes, as pixels with liquid water exhibit large biases

135   even if the signal at 37 GHz is mostly sensitive to snow (Derksen et al., 2012). For CB, an area with the same spatial coverage but a slightly different location was used since the snow pit area was within 25 km (full resolution of SSMIS) from the ocean. T_B were temporally averaged to match times of field measurements, representing peak winter snow accumulation (Table 2). Also, T_B were corrected for atmospheric contributions using the linear relation with precipitable water from the 29 atmospheric NARR layers (Vargel et al., 2020; Roy et al., 2013).

140

A multi-layered snowpack radiative transfer model (SMRT, Picard et al., 2018) was used to simulate snow emission at 19 and 37 GHz. Model inputs are snow temperature, density and microstructure of each snow layer. Correlation length of snow microstructure in each layer was estimated from mean density and SSA measurements of each layer when available (wind slab: WS and depth hoar: DH) using Debye's equation scaled by a factor ($\kappa_{37} = 1.39, \kappa_{19} = 1.71$) for arctic snow as suggested

145   by Eq. (3b) and (4) in Vargel et al. (2020) with the Improved Born Approximation (IBA-Exp) configuration. Soil emission was simulated using the Wegmüller and Mätzler (1999) model with permittivity and roughness values from a field study of frozen soil emission based in CB (Meloche et al., 2020). The soil parameters from CB (Meloche et al., 2020) closely match values from a study in TVC (King et al., 2018) and were used for both sites simulation. The lakes in CB shown in Figure 1 were not considered in the soil emission contribution because most of the water was frozen ($\varepsilon' \approx$ 4-6) (Mironov et al., 2010),

150   which had a similar permittivity to frozen soil ($\varepsilon' \approx$ 2-4) (Mavrovic et al., 2021) than liquid water ($\varepsilon' > 25$).

The basal layer temperature was set to the mean soil-DH interface measurements from snow pits of each site. The temperature of the WS layer was estimated from the North American Regional Reanalysis (NARR) air surface temperature, which closely matched snow pit surface layer temperature. NARR air surface temperatures were used because it provides a global estimate

155   that matches spatial coverage of the EASE grid, which is continuous (spatially and temporally) compared to the sparse snow pit observations.

160

Table 2: Summary of mean basal and air surface temperatures for SMRT simulations, precipitable water (PWAT) used for atmospheric correction and measured (corrected) T_B at both polarization vertical (V) and horizontal (H) by the SSMIS sensor (platform F18).

Sites	T_{base} (K)	$T_{surface}$ NARR (K)	PWAT (mm)	T_B 37H (K)	T_B 37V (K)
CB (April 15-29, 2019)	257	261.5	3.61	195.3	211.0
CB (April 12-24, 2018)	257	260.1	3.72	179.3	195.7
CB (May 1-8, 2017)	263	261.3	3.33	187.1	205.0
CB (April 2-10, 2016)	256	258.8	2.80	190.1	215.4
CB (April 9-16, 2015)	254	256.2	2.34	193.0	215.9
TVC (March 15 -25, 2019)	266	261.8	7.04	177.0	199.5
TVC (March 15 -23, 2018)	264	261.8	4.21	176.6	197.6

2.4 Gaussian Processes

Gaussian Processes (GP) are a non-parametric Bayesian method used in regression models. These processes are effective and flexible tools to fit complex functions with small training datasets (Quiñonero-Candela and Rasmussen, 2005). Gaussian processes provide uncertainties on predictions, using training data and prior distributions to produce posterior distributions for predictions. Mean ($m(x)$) and covariance ($k(x, x')$) functions from the multi-variate Gaussian distribution are used to fit data (x: snow depth, y: ratio of layer, DHF). The $m(x)$ function describes the expected value of the distribution and the $k(x, x')$ describes the shape of the correlation between data points (x_i). Different mean and covariance kernels can be chosen to fit the data. From Bayes rule in Eq. (1) where y (DHF) and X (snow depth) are observed data and f the GP function, posterior predictions of DHF can be produced. Posterior predictions were calculated using the standard method of Markov Chain Monte Carlo (MCMC) sampling using PyMC3 (Salvatier et al., 2016).

$$Posterior = \frac{Likelihood \cdot Prior}{Marginal\ likelihoo} \quad = \quad p(f|y,X) = \frac{p(y|X,f) \cdot p(f)}{p(y|X)} \tag{1}$$

$$f(x) \sim GP\ (m(x), k(x, x'), \phi(x)) \tag{2}$$

Equation 2 defined f as a function of $m(x), k(x, x')$. A mean function $m(x)$, following an inverse logic function (ϕ) (Eq. 3), was chosen due to the close fit with observations. The covariance function $k(x, x')$ is a Gaussian white noise covariance function and is defined with noise (σ) and the Kronecker delta function ($\delta_{x,x'}$) (Eq. 4), to best fit the observations. By using a scaling function (ϕ), the covariance function (uniform noise in this case) can be modified as a function of x. The scaling function used is also an inverse logic function (ϕ) that takes the same form as Equation 3. Finally, a deterministic transformation is applied to the prior (GP) to constrain values to a ratio (0,1). The likelihood of DHF observations is defined by a Beta distribution (0,1).

$$m(x) = \phi(x) = c + b\left[\frac{e^{a(x-x_0)}}{1+e^{a(x-x_0)}}\right] \tag{3}$$

185 $\quad k(x,x') = \sigma^2\delta_{x,x'}\phi(x) \tag{4}$

3. Results

3.1. Snow depth distribution

Distributions of snow depth are needed when integrating over large areas to calculate sub grid snow variability for distributed models (Clark et al., 2011; Liston, 2004). The μ_{sd} and the CV_{sd} of snow depth are used as parameters in probability density

190 functions to estimate the shape of the log-normal and gamma distributions. To find which distribution best fits the depth observations, we tested the log-normal and gamma distributions using the Kolmogorov-Smirnov two sample test with snow depth observations (shown in blue in Figure 2). The statistical fits for each distribution are shown in Table 3. For both the log-normal and gamma distributions the null hypothesis is validated at the 5% significance level from p-value > 0.05 (i.e. the two samples were drawn from the same distribution), which agrees with previous assessments of Arctic snow (Clark et al., 2011;

195 Gisnas et al., 2016).

Table 3: Kolmogorov-Smirnov (KS) test for 2 samples of probability distribution function (PDF).

Site	PDF	KS stats	p-value
TVC	log-normal	0.029	0.41
	gamma	0.039	0.11
CB	log-normal	0.024	0.63
	gamma	0.017	0.95
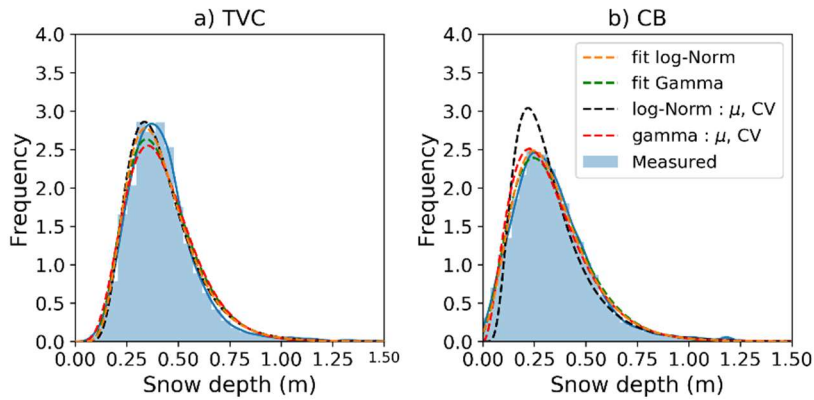
Figure 2: Log-normal and gamma distribution fit to the measured snow depths.

Distributions with parameterization using measured μ_{sd} and CV_{sd} (Figure 2) differ from the best fit with regular parameters, especially compared with log-normal distribution in CB (black dashed line in Figure 2b). Liston (2004) reported CV_{sd} of 0.4 for Arctic tundra snow, which is in close agreement with the values of 0.43 for TVC and 0.56 for CB. These values were obtained from spatially distributed snow depth measurements around snow pits. For comparison, maps of snow depth from RPAS for TVC (n = 6 325 365 with total spatial coverage of 5.3 km^2) showed a much larger CV_{sd}= 0.78 than magnaprobe data (n=15 731) with CV_{sd} = 0.43 (Table 4). A RPAS dataset was also available for CB but with a much smaller spatial coverage (0.2 km^2) showing a CV_{sd} of 0.49. In Figure 4, we investigated the relationship between spatial coverage of sampling and the CV_{sd} parameter. Datasets include RPAS-derived data at TVC (TVC18-RPAS) containing 6 areas with various size from 1- 3 km^2, CB18-RPAS map of 0.2 km^2 and the larger Lidar-derived snow map in TVC (TVC13-Lidar). Figure 3a shows snow accumulation of TVC13-Lidar and TVC18-RPAS with snow drift visible in dark blue and sub-grid of 1 km^2 showed areas with high CV$_{sd}$ (Figure 3b) containing more drift. For both areas, 500 Monte Carlo simulations were performed by randomly selecting sub-regions within each domain (Figure 4) so the mean and variability as a function of coverage could be investigated. Simulations showed sub-sampling of μ$_{sd}$ and CV$_{sd}$ converged to the values of the full area. The mean of each area was similar in value with less variation in the simulations compared to CV$_{sd}$. A difference of 0.2 between the full CV$_{sd}$ of the RPAS (5 km^2) and Lidar (93 km^2) maps (Figure 4) was found. Also included in Figure 4 are in-situ CV$_{sd}$ estimate with variable high-density sampling (magnaprobe) over different spatial extents at Daring Lake, NWT (Derksen et al., 2009; Rees et al., 2014), Puvirnituq, QC (Derksen et al., 2010) and at Eureka, NU (Saberi et al., 2017). The two points at the limit coverage scale correspond to areas of respectively 625 km2 (CV$_{sd}$ = 1; Daring Lake site; C. Derksen personal communication) and 198 km^2 (CV$_{sd}$ = 0.89, Eureka site; Saberi et al., 2007).

Table 4: Statistical parameters of snow depth distributions.

Site	n	μ (m)	σ (m)	CV_{sd}
TVC19	8 541	0.44	0.14	0.33
TVC18	7 190	0.39	0.21	0.54
TVC	**15 731**	**0.42**	**0.19**	**0.43**
TVC18-RPAS	**6 325 365**	**0.46**	**0.36**	**0.78**
TVC13-Lidar	**969 168**	**0.40**	**0.23**	**0.58**
CB19	982	0.42	0.17	0.40
CB18	577	0.34	0.18	0.53
CB18-RPAS	**7290**	**0.39**	**0.19**	**0.49**
CB17	4 045	0.42	0.19	0.46
CB16	3 403	0.28	0.16	0.61
CB15	12 282	0.32	0.18	0.57
CB	**20 712**	**0.36**	**0.18**	**0.52**
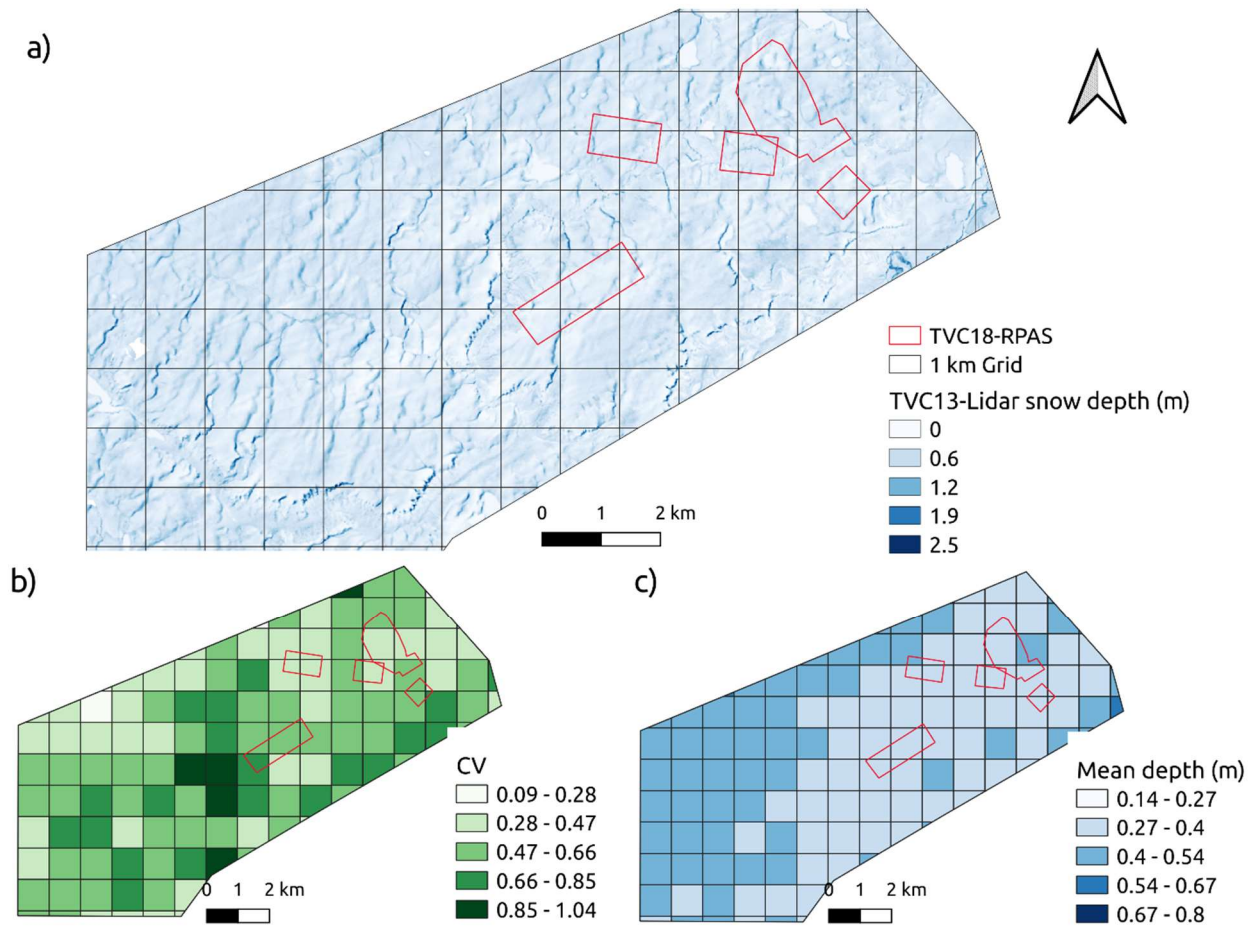
Figure 3: RPAS and Lidar dataset of snow depth at TVC (TVC13-Lidar and TVC18-RPAS). TVC13-Lidar is the largest dataset covering 93 km². TVC18-RPAS is a smaller dataset within the area of TVC13-Lidar. In a) is shown the snow depth map at 10 m resolution from 2013. b) shows a sub grid of 1 km with CV_{sd} for each cell; c) same as b) but for μ_{sd}.

225
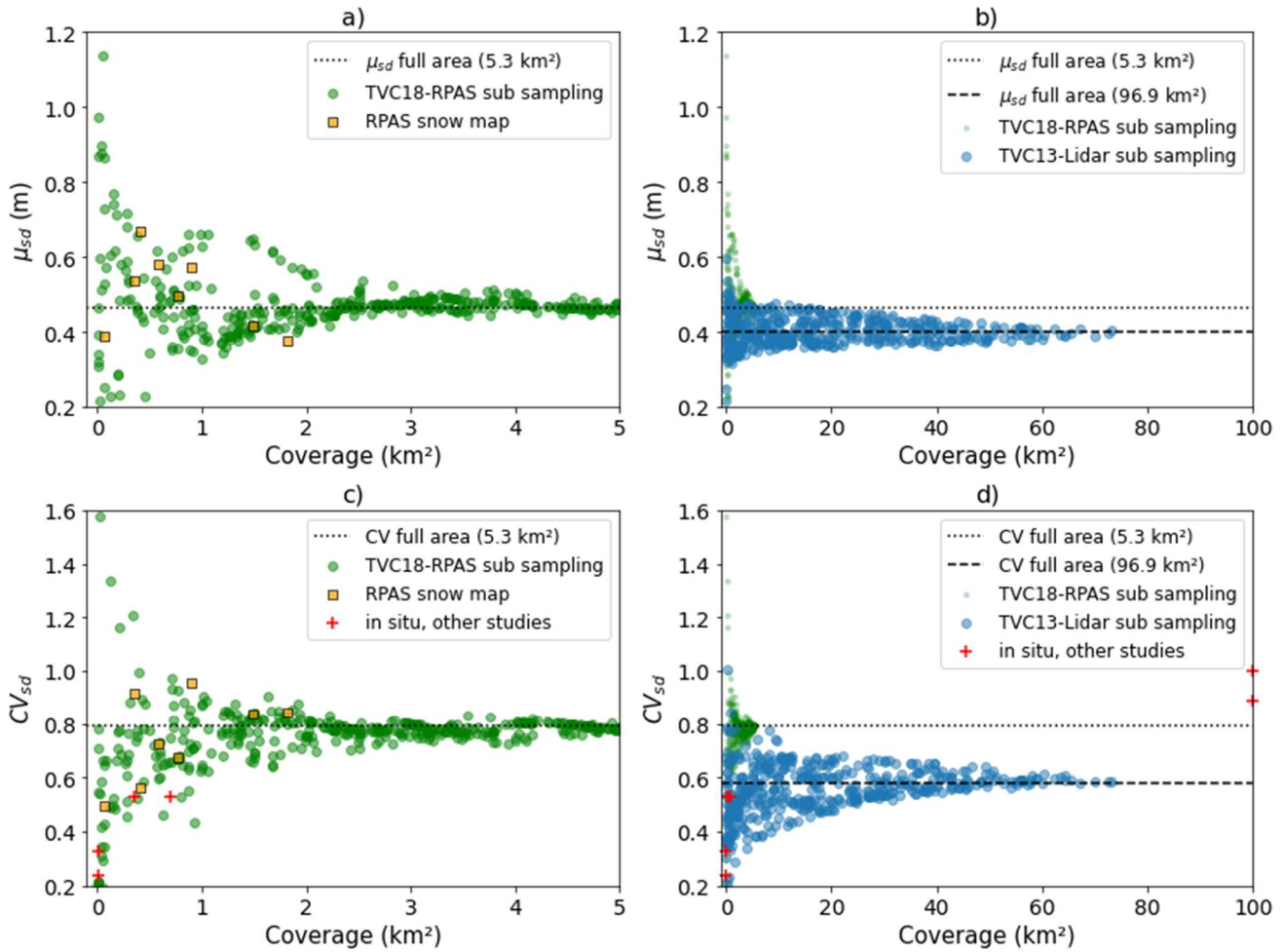
Figure 4: Snow depth mean (μ_{sd}) (a and b) and variability (CV_{sd}) (c and d) as a function of coverage for sampling area: a) and c) small area, b) and d) large area. Monte Carlo simulations were done using the two datasets in TVC. CB18-RPAS was also added in a) and c) because of the similar coverage. The μ_{sd} and CV_{sd} of both full areas are shown by the black dotted and dashed line.

3.2. Analysis of SSA and density per layer

After combining measurements from all snow pits at TVC and CB (n = 315) the mean proportion of DH layer thickness was 46% and WS was 54%. The goal was to classify DH as large grain snow (large facets, depth hoar cups and chains), then all other snow layers above the DH as wind slab (WS). Some layers were more difficult to classify as they contained mixed crystals or were a transitional slab-to-hoar layer (also referred to as indurated hoar) (Sturm et al., 2008). Slab that contained small faceted crystals (< 2 mm) were classified as WS. Indurated hoar, a wind slab metamorphosed into depth hoar, was classified into DH with a typical density ~ 300 kg · m^{-3}. Because of this reason, the peak of each distribution appeared close

to each other in Figure 5 c) and d). For retrieval of snow properties using satellite remote sensing, a 2 layer model using WS and DH can be used to simplify much of the layer complexity found in arctic snowpacks (Rutter et al., 2019; Saberi et al., 2017). A small amount of surface fresh snow (SS) was present in some pits but was not included in this calculation as this type of snow was a short-lived layer, combining fresh precipitation that rapidly transformed into rounded grains due to destructive metamorphism and defragmentation by wind. Distributions of SSA are more distinct between layers then density (Figure 5a and b), c.f. Rutter et al. (2019). Figure 5 c) and d) show that the mean values for density of WS (335 kg·m^{-3}) and DH (266 kg·m^{-3}) were closer together. SSA distributions also showed a gap between both mean values (WS: 19.7 m^{2}kg^{-1} and DH: 11.1 m^{2}kg^{-1}) (Figure 5, Table 5). Even if snow properties can show high heterogeneity at local scales, simple distributions approximate this variability well. Temporal (year) and spatial (regional between site) variation is low and snow properties (density and SSA) can be approximated by a distribution for each distinct layer, WS and DH as in Figure 5. Therefore, snow properties were simplified in distributions for each layer (WS and DH) representing tundra snow.
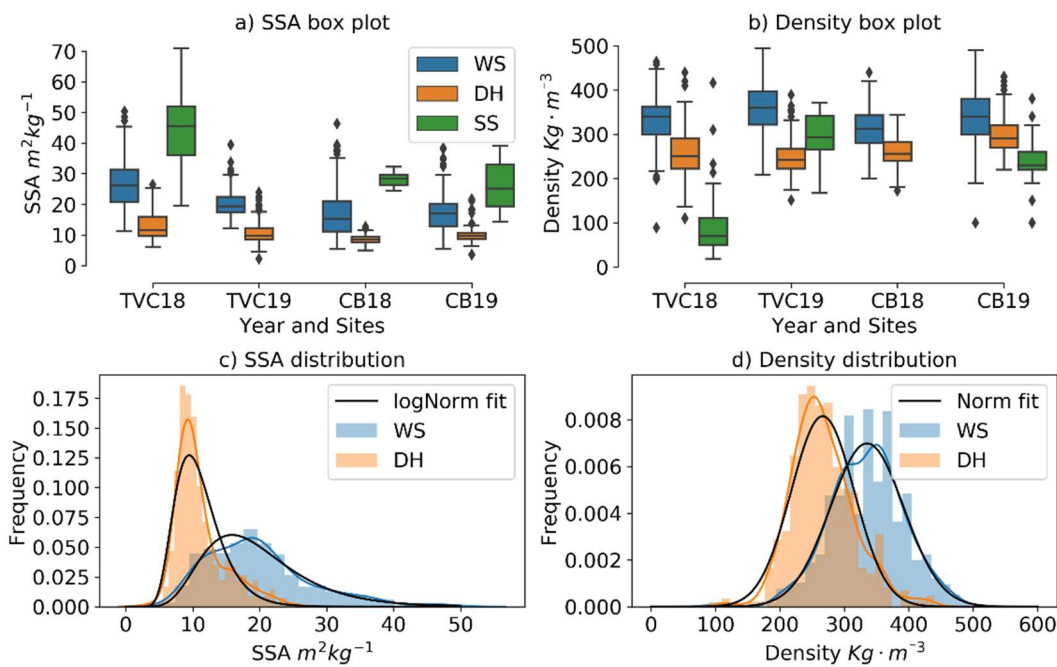
Figure 5: SSA and density variability of Surface Snow (SS), Wind Slab (WS) and Depth Hoar (DH) for the two studied sites (TVC and CB) and different dates (see Table 5). In c) the best log-normal fit distribution is shown in black; d) same as c) but for the normal fit distribution. In c) and d), the kernel density estimates (KDE) of the histogram of each layer are also shown (in color).

Table 5: Parameters for best fitting distribution of SSA and density for layers of DH and WS.

Snow property	Best fit PDF		μ	σ
SSA ($m^2 kg^{-1}$)	log-normal	DH	11.1	3.8
		WS	19.7	7.8
			μ	σ
Density ($kg\ m^{-3}$)	normal	DH	266.3	48.9
		WS	335.2	57.1

260

Parr et al. (2020) found a key threshold of $\mu_{sd} + 1\sigma_{sd}$ to define snow drifts in tundra environments. This threshold > 0.6 – 0.8 m, based on data presented in Table 4, is an important metric in Figure 6 since above this depth, the variability and the mean DHF is greatly reduced as the snowpack is dominated by wind slab for larger depth (drift). As defined in Parr et al. (2020), the transported snow from wind accumulates at these particular locations (drift) where it was scoured from wind

265   affected area yielding lower depth with high DHF.
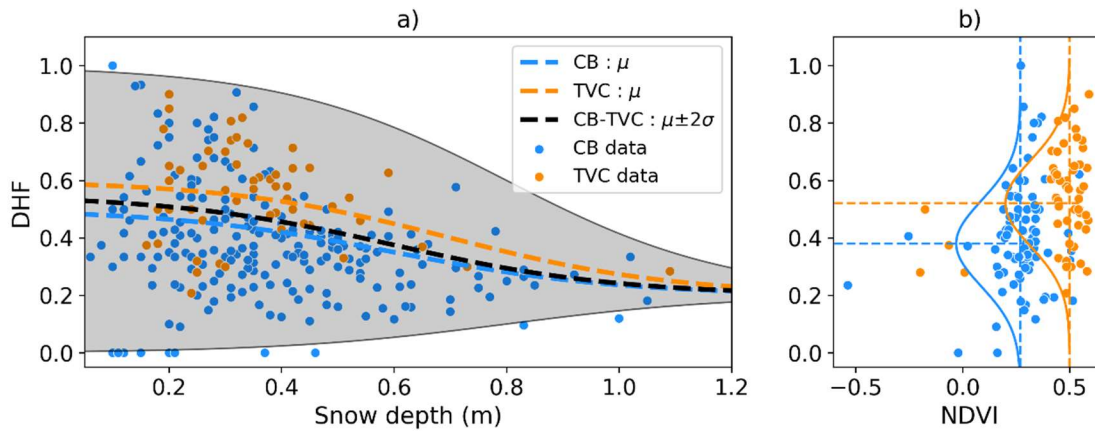
Figure 6: a) Depth hoar fraction (DHF) as a function of total depth for snow pit data from 2015-2019 in Cambridge Bay and 2018-2019 for Trail Valley Creek. Both datasets were separated in equal bins (10 cm) to estimate the mean value shown with dashed
270   **line. The black line represents the mean for both site with the 95% interval. b) DHF is shown as a function of NVDI from the snowpit area with the mean DHF and NDVI per sites shown by dashed lines and the gaussian distributions of DHF by the solid lines.**

Vegetation also strongly influences variability of DHF in shallower snowpacks, where arctic shrubs and tussocks promote
275   depth hoar formation (Domine et al., 2016; Royer et al., 2021; Sturm et al., 2001). However, there is no clear link between DHF and NDVI (a proxy for vegetation type) at local scales (Figure 6b). Since shrubs provide shelter to snow up to their own height (Gouttevin et al., 2018), vegetation height rather than type would be required. However, at the regional scale,

differences were evident between both regions, where mean NDVI and DHF are greater at TVC (NDVI = 0.5, DHF = 0.54) than CB (NDVI = 0.27, DHF = 0.38). This finding is in agreement with Royer et al. (2021) over a northeastern latitudinal
280 gradient, showing that sites with shrubs and tussocks have a greater DHF than those without.

3.3. DHF predictions using snow depth with Gaussian Processes

The impact on microwave scattering of variability of layer microstructures with snow depth was previously accounted for in Saberi et al. (2020) by defining two categories, a high scattering thin snow layer (high DHF) and a thicker self-emitting layer
285 (low DHF). Instead, using GP, DHF were fitted and predicted based on snow depth values (Figure 7). In order to use GP, the mean function $m(x)$, following an inverse logic function (ϕ_1: Eq. 3), was chosen with parameters: a = -5, x_0 = 0.6, b = 0.35 and c = 0.2 to best match the mean line observation for both sites in Figure 6. The mean function set the mean value across the snow depth range. The correlation function was set to a uniform noise, but this noise was reduced from depth > 40 cm by using a scaling function (ϕ_2: a=-5, x_0 = 0.6, b = 1.5 and c = 0.25). An inverse logic function (ϕ_1, ϕ_2) was used twice in the fitting
290 1) for the mean value and 2) to reduce the variability (noise) as snow depth increased. The snow pit dataset (n=315, Figure 6) was used to build posterior predictions using MCMC sampling.

For prediction of DHF, any number of snow depths can feed into the posterior prediction or GP fit. Snow depths were generated from a log-normal distribution with parameters (μ_{sd}, CV_{sd}) from previous section in Table 4. Posterior predictions of DHF were similar to observed data (Figure 7) and followed closely posterior probability representation in red (GP fit). Again, higher
295 variability in DHF was reproduced for depths < 0.5 m, which was then reduced for depths > 0.5m following the red posterior prediction representation in Figure 7.
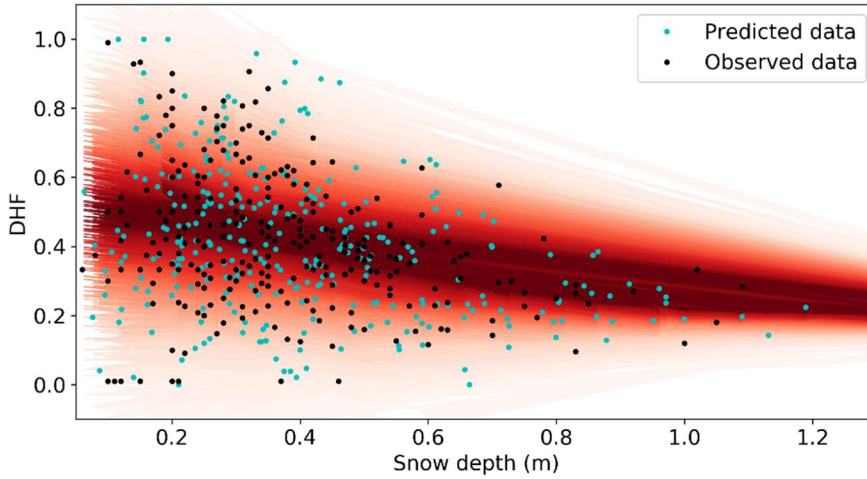
Figure 7: Prediction on DHF (cyan) using a GP fit trained on observed data (black). Snow depth were samples from a log-normal distribution with parameters from Table 4. The GP fit is illustrated in red where darker red represents high posterior probability that follows the mean function.

3.4. SMRT simulation of sub-grid variability within sensor footprint

SMRT simulations using measured snowpack properties were compared with the satellite measurements of T_B. Two simulations were evaluated using: 1) mean measured depth, each layer's density and SSA, and DHF, and 2) a log-normal distribution of snow depth and the GP fit (predicted DHF). We hypothesized that the EASE 2.0 grid pixel can be separated into n smaller sub-grid pixels. Sub-grid pixels (n = 500) represent the observed snow variability, where n snow depths will follow a log-normal distribution with parameters μ_{sd} and CV_{sd}. The ratio of each layer is predicted using the GP fit with depth as input from the log-normal distribution. Mean SSA (DH: 11 m^2kg^{-1}, WS: 20 m^2kg^{-1}) and density (DH: 266 kg m^{-3}, WS: 335 kg m^{-3}) per layer were determined from measurements (Figure 5).

For one standard EASE-grid pixel, a distribution of sub-grid T_B were simulated to reproduce a realistic distribution of T_B within the radiometer footprint. This variability was derived from spatially distributed observations from snow pits and snow depths observation. Snow depths followed a log-normal distribution with the mean measured depth (μ_{sd}) of each region (Table 4) and a depth variability (CV_{sd}) that was evaluated from a range of 0.1 to 1. The GP mean function from Figure 7 was used to predict the DHF for each region. When using CV_{sd} = 0.7 , the simulated distribution showed a wide sub-pixel variability (± 40K) with a mean value of T_{B37V} = 194.7 K (blue line in Figure 8a), very close to the satellite-measured T_{B37V} of 196.5K (green dotted line in Figure 8a). In this case, the T_B value simulated from the mean measured snow depth and mean DHF was slightly lower (190.7 K, i.e., a bias of 5.8 K) (black dotted line in Figure 8a). To represent the signal measured by the sensor, the mean of the simulated T_B was chosen and it was assumed that the sub-pixels effect combined linearly at this scale. Because the

320   simulated T_{B37V} distribution was not exactly a normal distribution, it appeared that the mean T_B of this distribution increased when CV_{sd} increased (Figure 8b). This meant that snow depth variability (CV_{sd}) must be accounted for when estimating the average T_B at 37 GHz, in addition to the mean snow depth values. The influence of the GP simulation on the mean simulated T_{B37V} was approximately 10 K (Figure 8b) as CV_{sd} varies from 0.1 to 1. The addition of snow variability in simulation (Figure 8c and d) of 19 GHz has negligeable effect on T_{B19} and shows a constant simulation across the CV_{sd} range of 0.1 to 1.

325   Simulation of T_{B19} shows higher biases at horizontal polarization then vertical polarization.
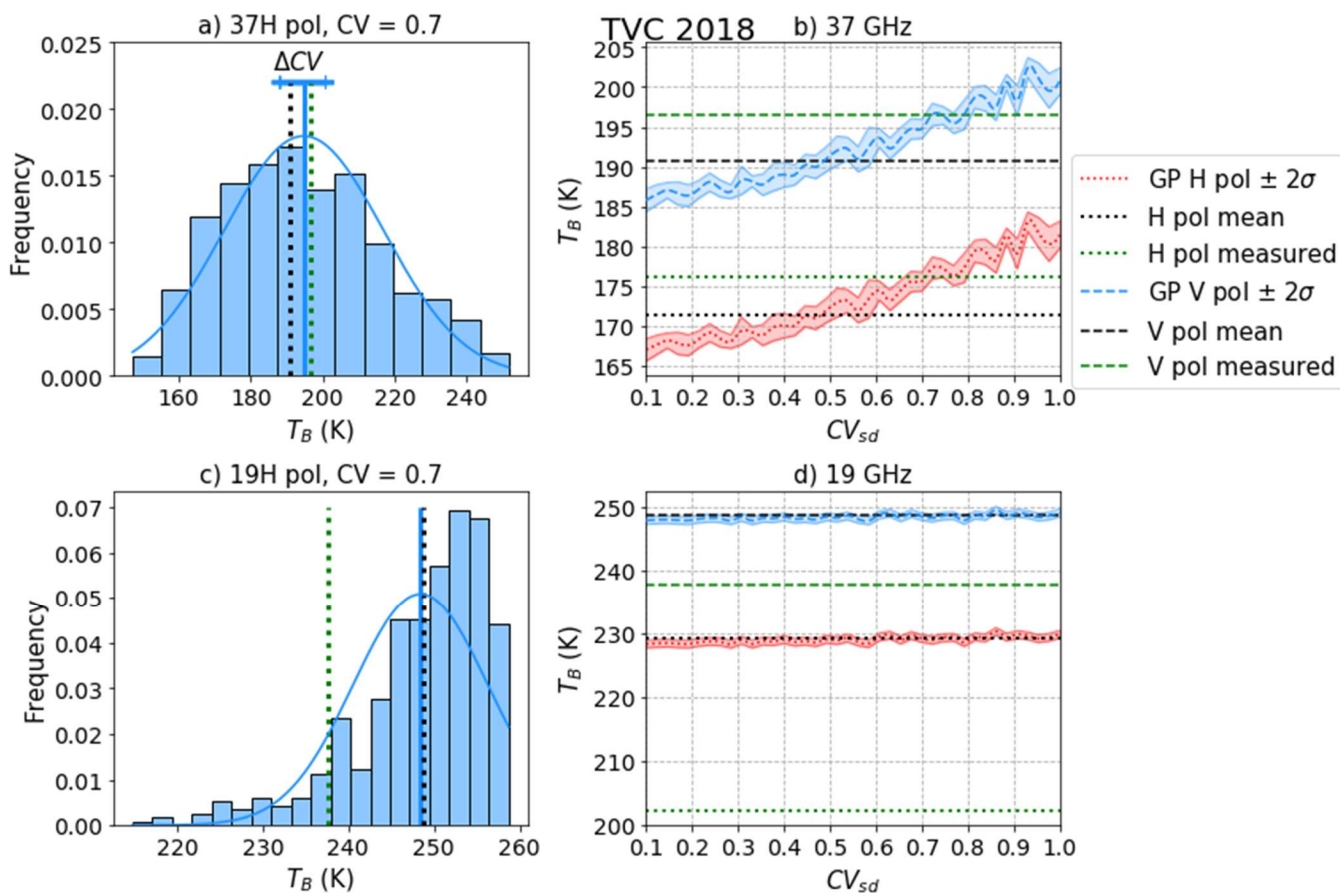
Figure 8: Brightness temperature variability simulation distribution, a) and c), of simulated T_B within a pixel, where vertical lines
330   **represent the mean of this distribution for V pol (blue), measured by satellite (green) and T_B value simulated from the mean measured snow depth and mean DHF (black). In b) and d), the mean of the simulated T_B for H pol (red) and V pol (blue) as a function of CV_{sd} with mean values (dotted black lines). The CV_{sd} that minimized biases is located at the red/blue-green intersection. Shaded blue and red areas correspond to a 2σ range representing uncertainty inherent from our Bayesian simulations in estimating the mean of simulated T_B for the pixel.**

335

GP simulation reduced biases by 5K with a higher optimized CV_{sd} (intersection of red/blue - green line, Figure 8b). A similar pattern was observed for CB (not shown here) but the measured T_B at CB was much higher than the GP simulation resulting in large bias for CB (~20K) compared to TVC (Table 6). Both sites suggested a larger CV_{sd}, which agreed with a CV_{sd} for larger spatial coverage measured in Figure 4. Observed large biases at CB vary over the years from 5K to 29K. The total

340   RMSE of both sites and years linearly decreased as a function of CV_{sd} (Figure 9). Total RMSE is minimized with higher CV_{sd} (0.8-0.9) typical of large sampling scale (over 4 km^2) as shown in Figure 4.

Table 6: Bias between SMRT simulated and measured Tb from SSMIS sensor at each site.

| | | Bias (K) | | | | RMSE (K) | |
| | | CB | | TVC | | | |
SMRT simulation type	Year	H pol	V pol	H pol	V pol	H pol	V pol
	2019	28.2	25.9	6.9	10.3	17.8	19.1
	2018	8.0	5.3	5.1	6.8		
mean depth and DHF	2017	19.9	18.9	-	-		
	2016	16.9	23.2	-	-		
	2015	24.7	29.1	-	-		
	2019	18.6	15.7	-4.4	-1.2	9.7	10.4
	2018	-3.7	-6.2	-4.9	-3.2		
GP simulation CV = 0.9	2017	10.4	9.3	-	-		
	2016	7.1	13.5	-	-		
	2015	10.0	13.9	-	-		

345
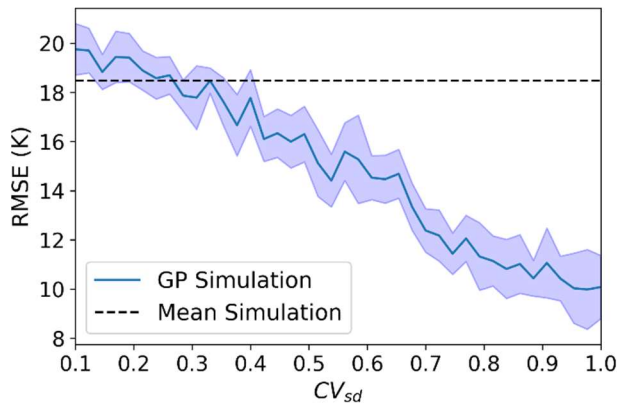
Figure 9: Overall RMSE (year and site) with the mean simulation (dashed black line) and the GP simulation in blue as a function of the coefficient of variation of snow depth.

4. Discussion

350 We show that as spatial coverage increased, the CV_{sd} parameter converged to the full area values (Figure 4). Monte Carlo simulations of snow depth distribution and coverage show high variation in CV_{sd} (from 0.1 to 2) for areas < 10 km². Snow accumulation varied at the meso scale (100 m to 10 km) due to topography and vegetation (Pomeroy et al., 2002) by varying wind-flow direction (Liston and Sturm, 1998). At the meso scale, variability in CV_{sd} was high due to topographic differences; plateau, slope and valley create favorable conditions from wind flow direction to promote snowdrift, scour and sublimation

355 processes (Parr et al., 2020; Rutter et al., 2019). Vegetation facilitates snow holding capacities by decreasing wind speed near the ground within and downwind of shrub (Marsh et al., 2010; Sturm et al., 2001). Some areas include both extreme drifts and thin snow, resulting in high CV_{sd} (dark green areas in Figure 3b) which are commonly found in TVC (Walker et al., 2020). CV_{sd} was lower for areas without drifts (light green areas in Figure 3b). In areas > 10 km² (Figure 4d), variation in CV_{sd} was reduced and yielded higher values > 0.6.

360

Convergence to higher CV_{sd} as spatial coverage increased matched the PMW optimized values found in this study using GP simulation (0.8 – 1.0). Our analysis in Figure 4d showed that CV_{sd} of TVC13-Lidar converged to 0.6 at 93 km², but two in situ points from other studies at 625 km² had higher CV_{sd} (0.9-1) due to larger coverage or different site characteristics. This indicates that a CV_{sd} between 0.6-1.0 is more suitable to represent snow depth variability in SWE retrievals for PMW SWE

365 products at 25 km for the EASE GRID 2.0 and 625 km² for GlobSnow 3.0 (Pulliainen et al., 2020). For active sensors (resolution < 1 km), the high variability in CV_{sd} under 1 km² due to high variation in snow depth (Figure 4b) can affect back scattering since active sensor at Ku band is also sensitive to volume scattering (King et al., 2018). The need for prediction of μ_{sd} and CV_{sd} based on topography could become essential at these scales not only for microwave remote sensing but also to improve snow modelling or land data assimilation (Kim et al., 2021).

370

Spatial complexities of Arctic snowpacks can be adequately characterized with distributions of snow depth (Figure 2) and simplified by considering density and SSA of two main layers (Figure 5). Such simplifications could be potentially useful for satellite SWE retrievals across Arctic tundra regions. Since Bayesian SWE optimization needs a strong first guess from regional *a priori* information, multiple distributions of snow depth, density and SSA presented here can be used for tundra

375 type snow in MCMC sampling (Pan et al., 2017; Saberi et al., 2020). Additionally, a similar approach to our GP simulation can be added so the CV_{sd} parameter can also be used as *a priori* information with a distribution from 0.8 to 1, since it improved T_B RMSE by ~8K (Figure 9). This approach improved T_B simulation compared to using only mean values of snowpack properties by adding variability within the footprint. The CV_{sd} parameter (describing variation in snow depth) has a considerable effect on brightness temperature (10 K) when used as an effective parameter to account for sub-pixel variability

380 of snow depth. The amount of scatterers (snow grain and structure) within the radiometer's footprint is adjusted via the DHF predicted from snow depth (CV_{sd}). The relationship found in Figure 6 used to predict DHF (Figure 7) could also be used

deterministically with the mean function (ϕ_1) or with a linear relation of DHF decreasing from 50% to 20%. However, the Bayesian gaussian process was used because SWE retrievals are currently implemented in a Bayesian framework (Takala et al., 2011).

385

Considering that the difference between 19 and 37 GHz is used in SWE retrievals (Takala et al., 2011), using the CV_{sd} to account for variability of scatterers only affected simulation of 37 GHz with weak effect on 19 GHz (Figure 8). If standard deviation of snow increases (more drift) then relatively fewer large scatterers from depth hoar are present within the footprint due to a low DHF generally observed in large drifts. The net result is then an increase in T_B at 37 GHz resulting from an

390 increase in CV_{sd} (Figure 8).

This idea of modulating the amount of scatterers based of DHF prediction and a distribution of snow depth (μ_{sd} and CV_{sd}) can be extended to future active Ku-band mission (Garnaud et al., 2019; King et al., 2018) as it known that microwave spatial variability affects backscatter signal (King et al., 2015) and SWE retrievals (Vander Jagt et al., 2013). The CV_{sd} parameter is

395 proposed as an effective parameter to account for variability inside the grid cell, while the mean depth (μ_{sd}) is assimilated by in situ measurements at weather stations in data assimilation schemes (Takala et al., 2011), or by physical snow model (Larue et al., 2018). The CV_{sd} could be optimized or predicted using relationships with spatial coverage (Figure 4) and statistical topographic regression (Grünewald et al., 2013). Future works would need dataset covering large area where μ_{sd} and CV_{sd} could be investigated with topography in smaller sub areas.

400 **4. Conclusion**

This study evaluated the use of parameters controlling Arctic snow depth distributions to improve passive microwave SWE retrievals by characterizing tundra snow sub-pixel variability. In shrub and graminoid tundra environments, mean values of snow depths (μ_{sd} = 0.33 - 0.44 m) and coefficient of variations (CV_{sd} = 0.4 - 0.8) were similar to those previously reported in Arctic tundra (Derksen et al., 2014; Liston, 2004; Sturm et al., 2008). Monte Carlo simulations were applied to investigate μ_{sd}

405 and CV_{sd} as a function of spatial coverage. An increase in CV_{sd} matched increased spatial coverage of snow depth sampling, indicating that a higher CV_{sd} (0.6-0.9) is more suited to estimate snow depth variation at the 3.125 km resolution EASE-Grid 2.0. Also, simulations show high variation in CV_{sd} (> 0.9) for areas < 10 km^2 suggesting a need for topography-based prediction of μ_{sd} and CV_{sd} at this scale. The CV_{sd} is shown to be an effective parameter to account for snow depth variability in simulation of snow T_B. A two-layer snowpack model (depth hoar and surface wind slab), which simplifies snowpack properties into

410 distributions, was used to initialize the SMRT model via a GP fit of the DHF related to snow depth. DHF is fitted to snow depth using a Bayesian Gaussian Process, which accounts for variation in snow scattering using CV_{sd}. SMRT simulation was used successfully to simulate satellite T_B, but there is still substantial uncertainties in the simulated values which are likely

linked to microstructural properties not captured by SSA (Krol and Löwe, 2016). SMRT simulations of T_B were reduced by 8 K after optimizing CV_{sd} to higher values (0.8-1.0), thereby matching CV_{sd} of spatially distributed snow depth from TVC18 – RPAS accounting for variation in snow properties inside the footprint of satellite sensor. The CV_{sd} parameter is proposed as an effective parameter to account for variability inside the footprint to minimize the difference between microwave measurements and simulations in SWE retrievals algorithm. This would be beneficial to the data assimilation scheme of the European Space Agency: GlobSnow product (Takala et al., 2011) and to model large scale climate trend of tundra snow (Mortimer et al., 2020; Pulliainen et al., 2020).

Data and codes availability

Data and code for the gaussian process fit and GP simulation are available: https://github.com/JulienMeloche/Gaussian_process_smrt_simulation.

RPAS map and magnaprobe from TVC are available: https://doi.org/10.5683/SP2/PWSKKG.

Author contributions

JM: Formal analysis, Investigation and writing - original draft preparation, AL: Writing – review & editing, Supervision, Investigation, Funding acquisition and Resources, NR: Writing – review & editing, Supervision, Investigation, AR: Writing – review & editing, Supervision, Investigation, JK: Writing – review & editing, Data acquisition, BW: Writing – review & editing, Data acquisition, PM: Data acquisition, EW: Data acquisition

Acknowledgements

The authors would like to thank the entire GRIMP research team from Université de Sherbrooke and CHARS staff team for field work assistance from 2015-2019 in Cambridge Bay. We thank Phil Marsh (Wilfrid Laurier University), Chris Derksen and Peter Toose (Environment and Climate Change Canada) for logistics and field work at Trail Valley Creek Research Station. We also thank Victoria Dutch from Northumbria University for her help with dataset management of TVC. The authors would like to thank the reviewers and the editor, Carrie Vuyovich, for their help in improving this manuscript.

Financial support

This research was made possible thanks to the financial support of the Natural Sciences and Engineering Research Council of Canada (NSERC), Polar Knowledge Canada, the Canadian Foundation for Innovation (CFI), Environment and Climate Change Canada (ECCC), Fonds de recherche du Québec – Nature et technologies (FRQNT), Northern Scientific Training Program (NSTP) and research funding from Northumbria University, UK.

Competing Interests

The authors declare that they have no conflict of interest.

450

5. References

Brodzik, M.J., Long, D.G., Hardman, M.A., 2018. Best practices in crafting the calibrated, Enhanced-Resolution passive-microwave EASE-Grid 2.0 brightness temperature Earth System Data Record. Remote Sens. 10. https://doi.org/10.3390/rs10111793

455 Chang, A.T.C., Foster, J.L., Hall, D.K., Rango, A., Hartline, B.K., 1982. Snow water equivalent estimation by microwave radiometry. Cold Reg. Sci. Technol. https://doi.org/10.1016/0165-232X(82)90019-2

Clark, M.P., Hendrikx, J., Slater, A.G., Kavetski, D., Anderson, B., Cullen, N.J., Kerr, T., Örn Hreinsson, E., Woods, R.A., 2011. Representing spatial variability of snow water equivalent in hydrologic and land-surface models: A review. Water Resour. Res. 47. https://doi.org/10.1029/2011WR010745

460 Derksen, C., Lemmetyinen, J., Toose, P., Silis, A., Pulliainen, J., Sturm, M., 2014. Physical properties of Arctic versus subarctic snow: Implications for high latitude passive microwave snow water equivalent retrievals. J. Geophys. Res. Atmos. 119, 7254–7270. https://doi.org/10.1002/2013JD021264

Derksen, C., Sturm, M., Liston, G.E., Holmgren, J., Huntington, H., Silis, A., Solie, D., 2009. Northwest Territories and Nunavut snow characteristics from a subarctic traverse: Implications for passive microwave remote sensing. J.
465 Hydrometeorol. 10, 448–463. https://doi.org/10.1175/2008JHM1074.1

Derksen, C., Toose, P., Lemmetyinen, J., Pulliainen, J., Langlois, A., Rutter, N., Fuller, M.C., 2012. Evaluation of passive microwave brightness temperature simulations and snow water equivalent retrievals through a winter season. Remote Sens. Environ. 117, 236–248. https://doi.org/10.1016/j.rse.2011.09.021

Derksen, C., Toose, P., Rees, A., Wang, L., English, M., Walker, A., Sturm, M., 2010. Development of a tundra-specific snow
470 water equivalent retrieval algorithm for satellite passive microwave data. Remote Sens. Environ. https://doi.org/10.1016/j.rse.2010.02.019

Domine, F., Barrere, M., Morin, S., 2016. The growth of shrubs on high Arctic tundra at Bylot Island: Impact on snow physical properties and permafrost thermal regime. Biogeosciences 13, 6471–6486. https://doi.org/10.5194/bg-13-6471-2016

Domine, F., Picard, G., Morin, S., Barrere, M., Madore, J.-B., Langlois, A., 2018. Major Issues in Simulating some Arctic
475 Snowpack Properties Using Current Detailed Snow Physics Models. Consequences for the Thermal Regime and Water Budget of Permafrost. J. Adv. Model. Earth Syst. https://doi.org/10.1029/2018MS001445

Durand, M., Liu, D., 2012. The need for prior information in characterizing snow water equivalent from microwave brightness

temperatures. Remote Sens. Environ. 126, 248–257. https://doi.org/10.1016/j.rse.2011.10.015

Fierz, C., Armstrong, R.L., Durand, Y., Etchevers, P., Greene, E., McClung, D.M., Nishimura, K., Satyawali, P.K., Sokratov, S. a., 2009. The international classification for seasonal snow on the ground. UNESCO, IHP–VII, Tech. Doc. Hydrol. No 83; IACS Contrib. No 1 80.

Gallet, J.C., Domine, F., Zender, C.S., Picard, G., 2009. Measurement of the specific surface area of snow using infrared reflectance in an integrating sphere at 1310 and 1550 nm. Cryosphere 3, 167–182. https://doi.org/10.5194/tc-3-167-2009

Garnaud, C., Bélair, S., Carrera, M.L., Derksen, C., Bilodeau, B., Abrahamowicz, M., Gauthier, N., Vionnet, V., 2019. Quantifying Snow Mass Mission Concept Trade-Offs Using an Observing System Simulation Experiment. J. Hydrometeorol. 20, 155–173. https://doi.org/10.1175/jhm-d-17-0241.1

Gisnas, K., Westermann, S., Vikhamar Schuler, T., Melvold, K., Etzelmüller, B., 2016. Small-scale variation of snow in a regional permafrost model. Cryosphere 10, 1201–1215. https://doi.org/10.5194/tc-10-1201-2016

Gouttevin, I., Langer, M., Löwe, H., Boike, J., Proksch, M., Schneebeli, M., 2018. Observation and modelling of snow at a polygonal tundra permafrost site: Spatial variability and thermal implications. Cryosphere 12, 3693–3717. https://doi.org/10.5194/tc-12-3693-2018

Grünewald, T., Stötter, J., Pomeroy, J.W., Dadic, R., Moreno Baños, I., Marturià, J., Spross, M., Hopkinson, C., Burlando, P., Lehning, M., 2013. Statistical modelling of the snow depth distribution in open alpine terrain. Hydrol. Earth Syst. Sci. 17, 3005–3021. https://doi.org/10.5194/hess-17-3005-2013

Kelly, R., 2009. The AMSR-E Snow Depth Algorithm : Description and Initial Results. J. Remote Sens. Soc. Japan 29, 307–317. https://doi.org/10.11440/rssj.29.307

Kelly, R.E., Chang, A.T., Tsang, L., Foster, J.L., 2003. A prototype AMSR-E global snow area and snow depth algorithm. IEEE Trans. Geosci. Remote Sens. https://doi.org/10.1109/TGRS.2003.809118

Kim, R.S., Kumar, S., Vuyovich, C., Houser, P., Lundquist, J., Mudryk, L., Durand, M., Barros, A., Kim, E.J., Forman, B.A., Gutmann, E.D., Wrzesien, M.L., Garnaud, C., Sandells, M., Marshall, H.-P., Cristea, N., Pflug, J.M., Johnston, J., Cao, Y., Mocko, D., Wang, S., 2021. Snow Ensemble Uncertainty Project (SEUP): quantification of snow water equivalent uncertainty across North America via ensemble land surface modeling. Cryosph. 15, 771–791. https://doi.org/10.5194/tc-15-771-2021

King, J., Derksen, C., Toose, P., Langlois, A., Larsen, C., Lemmetyinen, J., Marsh, P., Montpetit, B., Roy, A., Rutter, N., Sturm, M., 2018. The influence of snow microstructure on dual-frequency radar measurements in a tundra environment. Remote Sens. Environ. 215, 242–254. https://doi.org/10.1016/j.rse.2018.05.028

King, J., Kelly, R., Kasurak, A., Duguay, C., Gunn, G., Rutter, N., Watts, T., Derksen, C., 2015. Spatio-temporal influence of tundra snow properties on Ku-band (17.2 GHz) backscatter. J. Glaciol. 61, 267–279. https://doi.org/10.3189/2015JoG14J020

Krol, Q., Löwe, H., 2016. Relating optical and microwave grain metrics of snow: The relevance of grain shape. Cryosphere

10, 2847–2863. https://doi.org/10.5194/tc-10-2847-2016

Larue, F., Royer, A., De Sève, D., Roy, A., Cosme, E., 2018. Assimilation of passive microwave AMSR-2 satellite observations in a snowpack evolution model over northeastern Canada. Hydrol. Earth Syst. Sci. 22, 5711–5734. https://doi.org/10.5194/hess-22-5711-2018

515   Liljedahl, A.K., Boike, J., Daanen, R.P., Fedorov, A.N., Frost, G. V., Grosse, G., Hinzman, L.D., Iijma, Y., Jorgenson, J.C., Matveyeva, N., Necsoiu, M., Raynolds, M.K., Romanovsky, V.E., Schulla, J., Tape, K.D., Walker, D.A., Wilson, C.J., Yabuki, H., Zona, D., 2016. Pan-Arctic ice-wedge degradation in warming permafrost and its influence on tundra hydrology. Nat. Geosci. https://doi.org/10.1038/ngeo2674

Liston, G.E., 2004. Representing subgrid snow cover heterogeneities in regional and global models. J. Clim. 17, 1381–1397.
520   https://doi.org/10.1175/1520-0442(2004)017<1381:RSSCHI>2.0.CO;2

Liston, G.E., Sturm, M., 1998. A snow-transport model for complex terrain. J. Glaciol. https://doi.org/10.1017/S0022143000002021

Mavrovic, A., Pardo Lara, R., Berg, A., Demontoux, F., Royer, A., Roy, A., 2021. Soil dielectric characterization during freeze-Thaw transitions using L-band coaxial and soil moisture probes. Hydrol. Earth Syst. Sci. 25, 1117–1131.
525   https://doi.org/10.5194/hess-25-1117-2021

Meloche, J., Royer, A., Langlois, A., Rutter, N., Sasseville, V., 2020. Improvement of microwave emissivity parameterization of frozen Arctic soils using roughness measurements derived from photogrammetry. Int. J. Digit. Earth 0, 1–17. https://doi.org/10.1080/17538947.2020.1836049

Mironov, V.L., De Roo, R.D., Savin, I. V., 2010. Temperature-dependable microwave dielectric model for an arctic soil. IEEE
530   Trans. Geosci. Remote Sens. 48, 2544–2556. https://doi.org/10.1109/TGRS.2010.2040034

Montpetit, B., Royer, A., Langlois, A., Cliché, P., Roy, A., Champollion, N., Picard, G., Domine, F., Obbard, R., 2012. New shortwave infrared albedo measurements for snow specific surface area retrieval. J. Glaciol. 58, 941–952. https://doi.org/10.3189/2012JoG11J248

Mortimer, C., Mudryk, L., Derksen, C., Luojus, K., Brown, R., Kelly, R., Tedesco, M., 2020. Evaluation of long-term Northern
535   Hemisphere snow water equivalent products. Cryosphere 14, 1579–1594. https://doi.org/10.5194/tc-14-1579-2020

Pan, J., Durand, M.T., Vander Jagt, B.J., Liu, D., 2017. Application of a Markov Chain Monte Carlo algorithm for snow water equivalent retrieval from passive microwave measurements. Remote Sens. Environ. 192, 150–165. https://doi.org/10.1016/j.rse.2017.02.006

Parr, C., Sturm, M., Larsen, C., 2020. Snowdrift Landscape Patterns: An Arctic Investigation. Water Resour. Res. 56.
540   https://doi.org/10.1029/2020WR027823

Picard, G., Sandells, M., Löwe, H., 2018. SMRT: An active-passive microwave radiative transfer model for snow with multiple microstructure and scattering formulations (v1.0). Geosci. Model Dev. 11, 2763–2788. https://doi.org/10.5194/gmd-11-2763-2018

Pomeroy, J.W., Gray, D.M., Hedstrom, N.R., Janowicz, J.R., 2002. Prediction of seasonal snow accumulation in cold climate forests. Hydrol. Process. 16, 3543–3558. https://doi.org/10.1002/hyp.1228

Proksch, M., Löwe, H., Schneebeli, M., 2015. Density, specific surface area, and correlation length of snow measured by high-resolution penetrometry. J. Geophys. Res. Earth Surf. 120, 346–362. https://doi.org/10.1002/2014JF003266

Pulliainen, J., 2006. Mapping of snow water equivalent and snow depth in boreal and sub-arctic zones by assimilating space-borne microwave radiometer data and ground-based observations. Remote Sens. Environ. 101, 257–269. https://doi.org/10.1016/j.rse.2006.01.002

Pulliainen, J., Luojus, K., Derksen, C., Mudryk, L., Lemmetyinen, J., Salminen, M., Ikonen, J., Takala, M., Cohen, J., Smolander, T., Norberg, J., 2020. Patterns and trends of Northern Hemisphere snow mass from 1980 to 2018. Nature 581, 294–298. https://doi.org/10.1038/s41586-020-2258-0

Quiñonero-Candela, J., Rasmussen, C.E., 2005. A unifying view of sparse approximate Gaussian process regression. J. Mach. Learn. Res.

Rees, A., English, M., Derksen, C., Toose, P., Silis, A., 2014. Observations of late winter Canadian tundra snow cover properties. Hydrol. Process. 28, 3962–3977. https://doi.org/10.1002/hyp.9931

Roy, A., Picard, G., Royer, A., Montpetit, B., Dupont, F., Langlois, A., Derksen, C., Champollion, N., 2013. Brightness Temperature Simulations of the Canadian Seasonal Snowpack Driven by Measurements of the Snow Specific Surface Area. IEEE Trans. Geosci. Remote Sens. 51, 4692–4704. https://doi.org/10.1109/TGRS.2012.2235842

Royer, A., Domine, F., Roy, A., Langlois, A., Marchand, N., Davesne, G., 2021. New northern snowpack classification linked to vegetation cover on a latitudinal mega-transect across northeastern Canada. Écoscience 00, 1–18. https://doi.org/10.1080/11956860.2021.1898775

Royer, A., Roy, A., Montpetit, B., Saint-Jean-Rondeau, O., Picard, G., Brucker, L., Langlois, A., 2017. Comparison of commonly-used microwave radiative transfer models for snow remote sensing. Remote Sens. Environ. 190, 247–259. https://doi.org/10.1016/j.rse.2016.12.020

Rutter, N., Sandells, M., Derksen, C., Toose, P., Royer, A., Montpetit, B., Langlois, A., Lemmetyinen, J., Pulliainen, J., 2014. Snow stratigraphic heterogeneity within ground-based passive microwave radiometer footprints: Implications for emission modeling. J. Geophys. Res. Earth Surf. 119, 550–565. https://doi.org/10.1002/2013JF003017.Received

Rutter, N., Sandells, M.J., Derksen, C., King, J., Toose, P., Wake, L., Watts, T., Essery, R., Roy, A., Royer, A., Marsh, P., Larsen, C., Sturm, M., 2019. Effect of snow microstructure variability on Ku-band radar snow water equivalent retrievals. Cryosph. 13, 3045–3059. https://doi.org/10.5194/tc-13-3045-2019

Saberi, N., Kelly, R., Pan, J., Durand, M., Goh, J., Scott, K.A., 2020. The Use of a Monte Carlo Markov Chain Method for Snow-Depth Retrievals: A Case Study Based on Airborne Microwave Observations and Emission Modeling Experiments of Tundra Snow. IEEE Trans. Geosci. Remote Sens. 1–14. https://doi.org/10.1109/TGRS.2020.3004594

Saberi, N., Kelly, R., Toose, P., Roy, A., Derksen, C., 2017. Modeling the observed microwave emission from shallow multi-

layer Tundra Snow using DMRT-ML. Remote Sens. 9. https://doi.org/10.3390/rs9121327

Salvatier, J., Wiecki, T. V., Fonnesbeck, C., 2016. Probabilistic programming in Python using PyMC3. PeerJ Comput. Sci. https://doi.org/10.7717/peerj-cs.55

580   Sturm, M., Derksen, C., Liston, G., Silis, A., Solie, D., Holmgren, J., Huntington, H., 2008. A Reconnaissance Snow Survey across Northwest Territories and Nunavut, Canada, April 2007.

Sturm, M., Holmgren, J., 2018. An Automatic Snow Depth Probe for Field Validation Campaigns. Water Resour. Res. 54, 9695–9701. https://doi.org/10.1029/2018WR023559

Sturm, M., McFadden, J.P., Liston, G.E., Stuart Chapin, F., Racine, C.H., Holmgren, J., 2001. Snow-shrub interactions in
585   Arctic Tundra: A hypothesis with climatic implications. J. Clim. https://doi.org/10.1175/1520-0442(2001)014<0336:SSIIAT>2.0.CO;2

Sturm, M., Wagner, A.M., 2010. Using repeated patterns in snow distribution modeling: An Arctic example. Water Resour. Res. 46, 1–15. https://doi.org/10.1029/2010WR009434

Takala, M., Luojus, K., Pulliainen, J., Derksen, C., Lemmetyinen, J., Kärnä, J.P., Koskinen, J., Bojkov, B., 2011. Estimating
590   northern hemisphere snow water equivalent for climate research through assimilation of space-borne radiometer data and ground-based measurements. Remote Sens. Environ. https://doi.org/10.1016/j.rse.2011.08.014

Tsang, L., Chen, C. Te, Chang, A.T.C., Guo, J., Ding, K.H., 2000. Dense media radiative transfer theory based on quasicrystalline approximation with applications to passive microwave remote sensing of snow. Radio Sci. https://doi.org/10.1029/1999RS002270

595   Vander Jagt, B.J., Durand, M.T., Margulis, S.A., Kim, E.J., Molotch, N.P., 2013. The effect of spatial variability on the sensitivity of passive microwave measurements to snow water equivalent. Remote Sens. Environ. 136, 163–179. https://doi.org/10.1016/j.rse.2013.05.002

Vargel, C., Royer, A., St-jean-rondeau, O., Picard, G., Roy, A., Sasseville, V., Langlois, A., 2020. Remote Sensing of Environment Arctic and subarctic snow microstructure analysis for microwave brightness temperature simulations.
600   Remote Sens. Environ. 242, 111754. https://doi.org/10.1016/j.rse.2020.111754

Walker, B., Wilcox, E.J., Marsh, P., 2020. Accuracy assessment of late winter snow depth mapping for tundra environments using Structure-from-Motion photogrammetry. Arct. Sci. 17, 1–17. https://doi.org/10.1139/as-2020-0006

Wegmüller, U., Mätzler, C., 1999. Rough bare soil reflectivity model. IEEE Trans. Geosci. Remote Sens. 37, 1391–1395. https://doi.org/10.1109/36.763303

605   Wiesmann, A., Mätzler, C., 1999. Microwave emission model of layered snowpacks. Remote Sens. Environ. https://doi.org/10.1016/S0034-4257(99)00046-2

Winstral, A., Elder, K., Davis, R.E., 2002. Spatial Snow Modeling of Wind-Redistributed Snow Using Terrain-Based Parameters. J. Hydrometeorol. 3, 524–538. https://doi.org/10.1175/1525-7541(2002)003<0524:SSMOWR>2.0.CO;2

Winstral, A., Marks, D., 2014. Long-term snow distribution observations in a mountain catchment: Assessing variability, time

610   stability, and the representativeness of an index site. Water Resour. Res. 50, 293–305. https://doi.org/10.1002/2012WR013038

Winstral, A., Marks, D., Gurney, R., 2013. Simulating wind-affected snow accumulations at catchment to basin scales. Adv. Water Resour. 55, 64–79. https://doi.org/10.1016/j.advwatres.2012.08.011

615